Immersed Boundary Wall-Modelled Large Eddy Simulations for Automotive Aerodynamics

Jordan B. Angel*, Aditya S. Ghate, Gaetan K. W. Kenway, Man Long Wong, and Cetin C. Kiris
Volcano Platforms Incorporated, Palo Alto, CA 94304, USA

Neil Ashton
Amazon Web Services, 60 Holborn Viaduct, London EC1A 2FD, UK

This paper presents preliminary validation results of a new immersed boundary Wall-Modelled Large Eddy Simulation (WMLES) framework, *Volcano ScaLES*, for two automotive configurations as part of the 4$^{\text{th}}$ Automotive CFD Prediction Workshop (AutoCFD 4): the Windsor Squareback body and the DrivAer Notchback model. For the Windsor body, grids of up to 363 million cells were run to assess the sensitivity to spatial resolution and showed favorable correlation to experimental pressure and velocity data. This paper also presents preliminary results for the simulation of the DrivAer model which more closely represents the complexity of a production road-vehicle. We assess the sensitivity to the sub-grid scale closure model as well as the influence of mesh refinement on solution accuracy by exploring grids of more than half a billion cells. For both cases we demonstrate how the use of WMLES based upon a Cartesian immersed boundary method built for GPUs from the ground-up can provide both excellent correlation to experimental data as well as computational efficiency; only requiring the use of desktop-grade GPUs such as the Nvidia GeForce RTX 4090 or A10g series. To the authors knowledge, this is one of the first examples of a WMLES using a Navier–Stokes based Cartesian finite-difference code with immersed-boundary method being used to simulate a complex road-vehicle.

I. Introduction

Stricter climate regulations and consumer demand has spurred efforts to improve fuel efficiency of internal combustion engines (ICE) as well as fueling the interest in electric vehicles. For both engine types, the aerodynamic properties of road-vehicles are a leading order effect in determining the range or fuel efficiency of the vehicle [1]. The aerodynamic performance is also often seen as a key differentiator between automotive brands and is therefore one of the critical performance targets when developing a new car.

Road vehicles exhibit several complex flow phenomena typical of bluff body flows and complex geometry that have similarities to those experienced in high-lift aircraft aerodynamics. Off-body vorticity with large regions of turbulent recirculation in the wake, boundary layer separation and reattachment, near ground boundary layer interaction, and laminar-to-turbulent transition that can be delicately affected by the local curvature of the vehicle exterior to name a few. Together these effects create a richly dynamic and immensely complicated flow field.

Computational Fluid Dynamics (CFD) is now a mainstream tool within the design process of all major automotive companies. It is used widely to explore initial concepts and more recently the increased use of scale-resolving methods such as those in the hybrid RANS-LES category (e.g Delayed Detached-Eddy Simulation [2]) has meant it is increasingly trusted for decisions later in the design process [3, 4]. However, even though there has been progress, there is still widespread use of wind-tunnels to certify final designs and to make key design decisions where CFD is not still trusted when the correlation of CFD to wind-tunnel or on-road data is poor.

In addition to accuracy, an additional factor for automotive companies is the computational cost and time of CFD simulations. Typically the time taken for the simulation to run on High-Performance Computing (HPC) facilities as well as the financial cost are limiting factors in the number of simulations that can be run. These factors also limit the accuracy of the simulation given the strong link between the time/cost of a simulation (e.g lower time-step, finer mesh and therefore longer run times) and the accuracy of a simulation.

The Automotive CFD Prediction Workshop (AutoCFD) was created in 2018 [5] to help academics and industry within the automotive CFD community to advance the state of the art in Computational Fluid Dynamics (CFD) for

*Corresponding author.

automotive aerodynamics and assess new methods that can help to improve accuracy and computational efficiency of road-car simulations. The workshop [5–7] provides benchmark cases for participants to test their simulation methods and compare results with experimental data. The work described in this paper is connected to the 4$^{\text{th}}$ Automotive CFD Prediction Workshop (AutoCFD 4) * where the test-cases are the Windsor Squareback body [7, 8] and the DrivAer Notchback model [9, 10] (with minor modifications to the notchback model, as discussed in Hupertz et al. [11]) .

The Windsor body [7, 8] is a simplified representation of a car with a blunt rear with no taper or slant, that was created to provide closer realism to road-cars compared to the Ahmed car body [12]. The DrivAer model is significantly more complicated and represents most of the complexity of a modern car. Submissions for the DrivAer case in the previous AutoCFD 3 workshop show large variability in the predicted drag, exceeding the test repeatability by a factor of 10 †. The workshop summary concluded there were observable differences between steady and unsteady approaches as well as variability between different turbulence closure models for so-called identical methods. Prediction accuracy within wind tunnel repeatability tolerance is desired, but for the workshop, emphasis is also placed on correctly predicting the difference between a baseline and modified design which is a necessary requirement for any useful design tool. Specifically, the DrivAer Notchback case has ‘a’ and ‘b’ variants with ‘Case 2a’ as the baseline model and ‘Case 2b’ having a Front Wheel Deflector (FWD) which is well-known by the automotive design community to reduce drag. Figure 2 shows two views of the geometry with the FWD installed, shown in red. Comparing the predicted drag differences between submissions shows clear sensitivity to modelling and solver choices. The areas most sensitive were the wheel wells and the rear of the vehicle where large flow separation and pressure gradients at high curvature corners of the vehicle create recirculation regions. These vortex structures may be design dependent which makes them important to capture accurately when assessing modifications since they contribute significantly to the drag.

In this paper we present preliminary results for both of the AutoCFD4 test cases from a new Cartesian immersed boundary Wall-Modelled Large Eddy Simulation (WMLES) framework, Volcano ScaLES, with a focus on evaluating the predictive accuracy and on the practicality of scale-resolving simulations for industrial automotive design processes. The paper is organised as follows: first, the numerical methods are described including details on the immersed-boundary method and spatial discretization schemes. Next, the results from each test-case are discussed in turn, focusing on both global force coefficients and also selected off-body quantities such as planes in the wake of the Windsor and Drivaer vehicles. Finally, conclusions are drawn and future work is described.

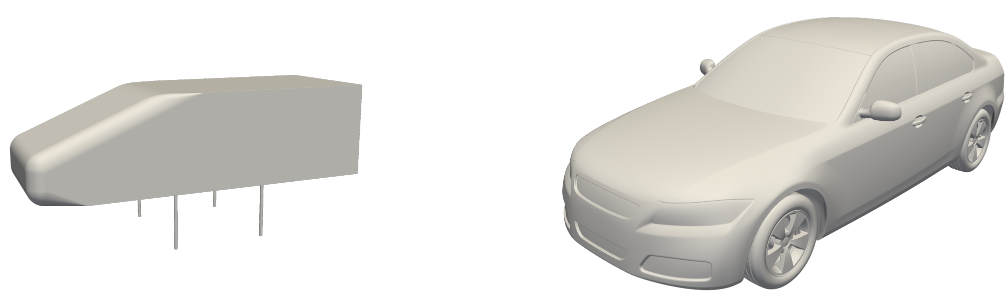

Fig. 1 Surface geometry for the two cases considered in this paper. Case 1 (left) considers the Windsor Squareback body, a simplified car model. Case 2 (right) considers two variants of the DrivAer Notchback body. The difference of these two variants is shown in Figure 2.

*https://autocfd.org

†https://autocfdv3.s3.eu-west-1.amazonaws.com/presentations/Th1105_AutoCFD3_Case2_Results_220421_PUBLISHED.pdf

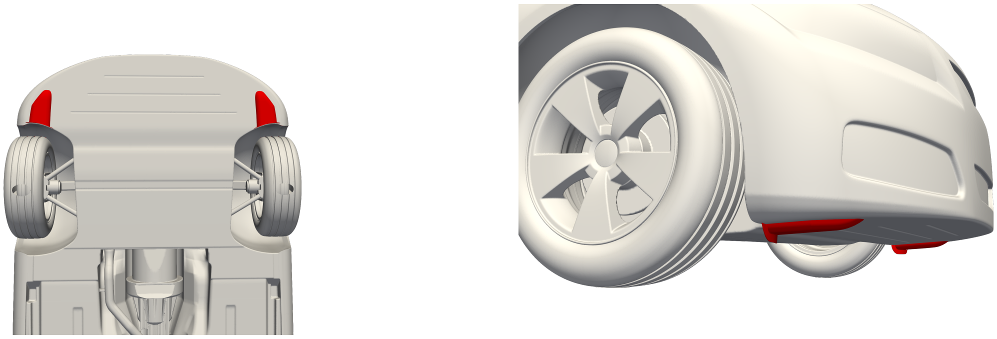

Fig. 2 Views of the DrivAer geometry showing the Front Wheel Deflector (FWD).

II. Numerical Method

A. Numerical formulation

Volcano ScaLES solves the compressible Navier–Stokes equations using a nominally fouth order spatially accurate finite difference discretization with favorable Kinetic Energy and Entropy Consistency properties making it suitable for Large Eddy Simulations (LES) over a range of flow regimes. The viscous flux discretization utilizes a mix of fourth order and second order discretizations with high spectral bandwidth thereby allowing further robustness for high Reynolds number flows without additional numerical dissipation via the inviscid flux numerical operator in turbulence resolving regions. Physics-based numerical sensors that are functions of local velocity gradients as well as pressure and density fluctuations allow for localized use of limiters needed to capture flows with discontinuities such as shocks and steep density gradients. A key convenience afforded by the use of Cartesian grids with unit aspect ratio is the use of explicit time-stepping scheme even in flows involving highly complex geometries; the perfectly isotropic grid cells near the geometry do not introduce any numerical stiffness associated with complex grid topologies. There are other significant advantages of Cartesian meshes including significantly reduced memory requirements for storing the grid as well as efficient and high accuracy in the underlying numerical formulation. The popular Strong Stability Preserving (SSP) variant of the classical third order Runge–Kutta scheme developed by Gottlieb and Shu [13] is utilized for all the work presented in this paper.

Geometries are represented in the numerical formulation using an immersed boundary algorithm capable of enforcing inviscid no-penetration boundary conditions as well as viscous skin friction with appropriate Reynolds number asymptotic properties using an equilibrium wall-model. The wall-model that provides a shear-stress constraint at the wall uses solution information interpolated via probing at a fixed distance of $3\Delta/2$ into the fluid away from walls. Additional methods to damp generation of spurious numerical noise at walls as well as at coarse-fine interfaces are also utilized in the present work. Simulations presented in this work utilize either the constant coefficient Vreman subgrid scale closure [14] or the dynamic Smagorinsky model [15, 16] to model the subgrid-scale stresses.

The CFD solver has been validated using a sequence of WMLES including: a) aerodynamics of iced straight wings [17], b) F-16XL aircraft aerodynamics [18], c) subsonic jets [19], d) airframe noise [20], and e) vibro-acoustics of a launch vehicle [21].

B. Octree Cartesian Grid System

The Volcano ScaLES solver uses Cartesian grids generated using a recursive octree approach. Grids around complex configurations consist of an unstructured tree-of-cubes with millions of leaf cubes each containing a structured grid of 8^3 or 4^3 cells. This method gives nearly all the computational advantages of structured grids while retaining the ability to closely follow surfaces and minimize the number of "dead" cells inside the geometry. Typically, 90-95% of the total cells in a grid are compute cells, while the remaining ones are considered "dead" or "blanked" cells.

C. Computational Architecture

Motivated by the need to fully exploit all available resources on modern GPUs, Volcano ScaLES is written exclusively in C++ and CUDA. On simulations involving non-canonical geometries such as those considered in this paper, we achieve approximately 30% of peak FLOPs on compute-oriented devices along with nearly perfect (>95%) weak scaling efficiency from 1 to 8 GPUs. Unlike most CFD codes, the majority of the computations are compute bound and we achieve high performance even in graphics-oriented, bandwidth-restricted devices, such as the Nvidia GeForce RTX 4090. The combination of Cartesian methods and an explicit time stepping scheme yields extremely low memory requirements: ScaLES can simulate between 8.5 and 10 million cells per gigabyte of GPU memory depending on the complexity of the configuration. Simulations containing between 400 and 500 million cells are routinely performed on desktop computers containing just two RTX 4090 GPUs with 24 Gb of memory each. The ability to fully exploit GPU hardware such as the Nvidia A10G accelerators on Amazon Web Services that offer better price-performance than more expensive Nvidia A100/H100-based hardware, significantly lower the cost of large eddy simulations to a level that is practical for use in an industrial setting.

III. Computational Results and Discussions

This section discusses the current results obtained for the 4th Automotive CFD Prediction Workshop (AutoCFD 4) Case 1 (Windsor body) and both Case 2 (DrivAer) variants. Section III.A considers a mesh refinement study of Case 1 using three grids. Comparisons of computed drag coefficient (C_d) to measured drag for each grid is given and a medium sized grid is selected for further validation comparisons including data from pressure taps and velocity data. Section III.B deals with both Case 2 variants. A matrix of simulations are carried out considering variations in subgrid scale model (Vreman or dynamic Smagorinsky model) and wall spacing (2 mm or 1 mm) for both 2a and 2b geometries for eight total simulations. It should be emphasized that these results are not considered finalized. At the ti me of writing, the workshop is ongoing and finalized results will be submitted to the AutoCFD 4 workshop.

A. Case 1: Windsor Body

The Windsor body is a car-like bluff body that has been used in numerous CFD studies as well as previous AutoCFD workshops. The Windsor body was designed as a case that captures relevant flow physics for road cars but is simple enough to be approachable for most CFD codes. Two variants of the Windsor body were experimentally tested at the Loughborough University wind-tunnel [8] and have been the subject of numerous CFD studies - that most recently have taken place within the 2nd, 3rd and 4th Automotive CFD Prediction Workshops [7]. The Windsor body was tested in numerous configurations but for this study we follow the AutoCFD4 setup, where the vehicle has no wheels (which simplifies a common source of uncertainty) and the squareback rear shape is used. For third and fourth AutoCFD workshops the Windsor body is yawed $-2.5°$ with respect to the wind tunnel. The Reynolds number is approximately 2.9×10^6 based on the body length and the freestream velocity. A nominal inlet velocity of $40\,\mathrm{m/sec}$ is given upstream of the car and a sensor is placed at $(x, y, z) = (-2\,\mathrm{m}, 0\,\mathrm{m}, 1.3\,\mathrm{m})$ to measure local static pressure and velocity. These are used to normalize the force and pressure coefficients. The domain required for this case (see Figure 3) represents the wind tunnel confinement but with the following modifications:

1) The Windsor body sidewalls are aligned with the mesh cells, the tunnel is yawed.
2) Only the ground plane has a no slip condition and hence has boundary layer growth; the top and side walls should be treated as a slip or 'inviscid' wall.
3) A long parallel inlet run is used in order to grow a boundary layer on the ground plane of approximately the correct thickness.
4) A parallel exit run is added downstream to avoid interactions with the wake. The domain extends upstream to $x = -5\,\mathrm{m}$ and downstream to $x = +6\,\mathrm{m}$ (the model is $x = -0.56\,\mathrm{m}$ nose to $x = +0.48\,\mathrm{m}$ base). The width and height of the CFD domain matches the wind tunnel.
5) To minimize numerical reflections from the tunnel exit, the tunnel was allowed to vent into the open air which is initialized with atmospheric conditions and given external flow boundary conditions far from the tunnel. This means there is no fixed pressure condition or any other boundary condition enforced at the tunnel exit.

Figure 4 depicts the mesh refinements regions on the slice $y = 0\,\mathrm{m}$ which is colored based on the grid spacing of the G_2 mesh in Table 1. Refinement is emphasized for the boundary layer development from the nose of the car and for the wake and off-body vorticity directly behind the body. An explanation of the grid refinement topology seen in Figure 4 is needed since the oversized wake block appears to be unnatural for the Windsor geometry. The grid refinement study presented in this section was carried out as a validation step before using the same grid topology to

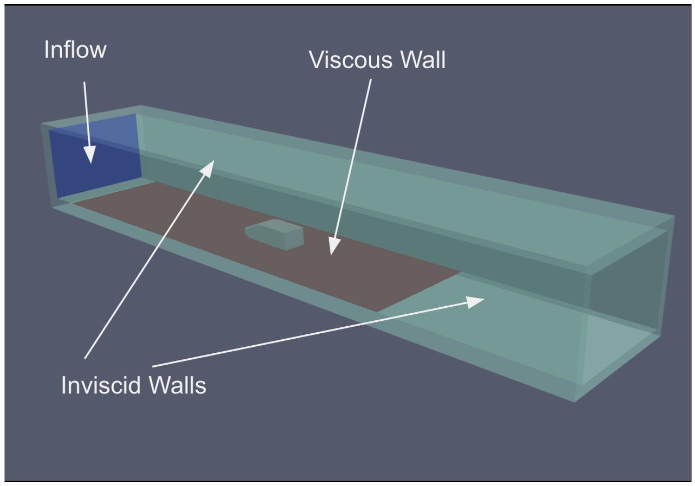

Fig. 3 Depiction of the computational domain for the Windsor body simulations.

simulate hundreds of geometric variations of the Windsor body as part of a study concerned with machine learning for automotive aerodynamics [22]. These geometric variations include many different ride heights and the authors chose to keep the grid topology fixed for all geometries which results in larger refinement regions. Using this refinement topology, we consider a consistent grid refinement study for the Windsor body. Table 1 shows results of a consistent grid refinement study using a sequence of grids $\{G_j\}$ for $j = 1, 2$ and 3. The columns of the table show the minimum grid spacing used, the number of computational cells in the grid, the wall-clock time per convective time unit[‡] (CTU) in minutes and the drag coefficient C_d. An additional row is included for the experimental drag coefficient value. Based on the results, G_2 is chosen as a representative case and the remainder of the experimental comparisons are carried out for the G_2 grid. This was to achieve a balance between accuracy, computational cost, and reach a mesh size that is typically used by the automotive industry for external aerodynamics.

Figure 5 and Figure 6 show pressure coefficient cuts for the planes $y = 0.0$ m and $z = 0.2595$ m respectively. The predictions are in good agreement with the experimental data however we observe some discrepancies in the z constant plane near the windshield area. The base pressure comparison in Figure 7 shows a similar pressure distribution as the experiment with a low pressure region on the leeward side of the vehicle associated with the recirculation region. Time-averaged streamlines colored by mean normalized streamwise velocity at $z = 0.195$ m are shown in Figure 8 compared with a figure from the thesis from Varney [23]. The streamlines show the large recirculation region behind the vehicle and the correct flow topology. The data for the $z = 0.195$ m slice was taken with a freestream velocity of 40 m/s which is the same as our simulation, but in addition to this plane, tomographic PIV was taken for a 3D region behind the car. This data was recorded for a flow with a freestream velocity of 30 m/sec. To make comparisons with the tomographic PIV data, we normalize the velocities by their freestream velocity. With that caveat, Figure 9 and Figure 10 show a comparisons of the normalized time average streamwise velocity for progressive cuts through the wake going downstream. The prediction are accurate in the wake region however the experiment seems to show a much larger shear layer near the car suggesting a much thicker boundary layer. Moving downstream, the predicted and experimental flow have essentially the same shear layer thickness. The overall shape of the wake region is well captured as well as its interaction with the floor boundary layer which can be seen in the velocity contours.

[‡]Nondimensional convective time unit is defined to be CTU = tU_∞/L where L is the length of the Windsor body.

Table 1 Computational cost for the Windsor body. All simulations were run using 8× NVIDIA A10g (Amazon EC2 g5.48xlarge) GPUs.

Label	Min. grid spacing [mm]	No. of compute cells [M]	Wall time / CTU [min]	C_D [-]
G_1	1.00	151	6	0.31
G_2	0.75	275	15	0.34
G_3	0.625	468	27	0.33
Exp.	-	-	-	0.33

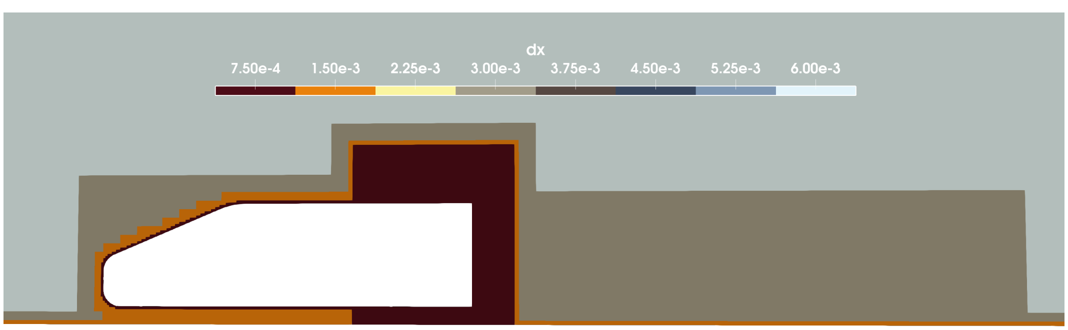

Fig. 4 Grid spacing for a slice through $y = 0.0\,\mathrm{m}$ for the Windsor body.

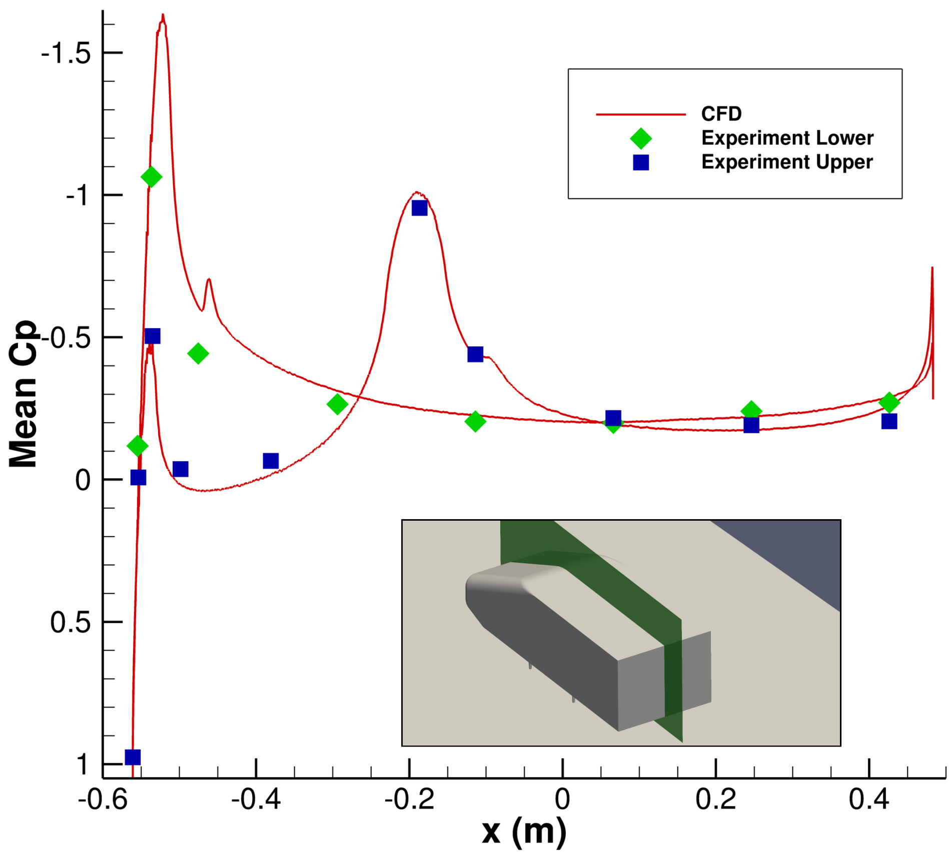

Fig. 5 Comparison of mean pressure coefficient at $y = 0\,\mathrm{m}$ for the Windsor body.

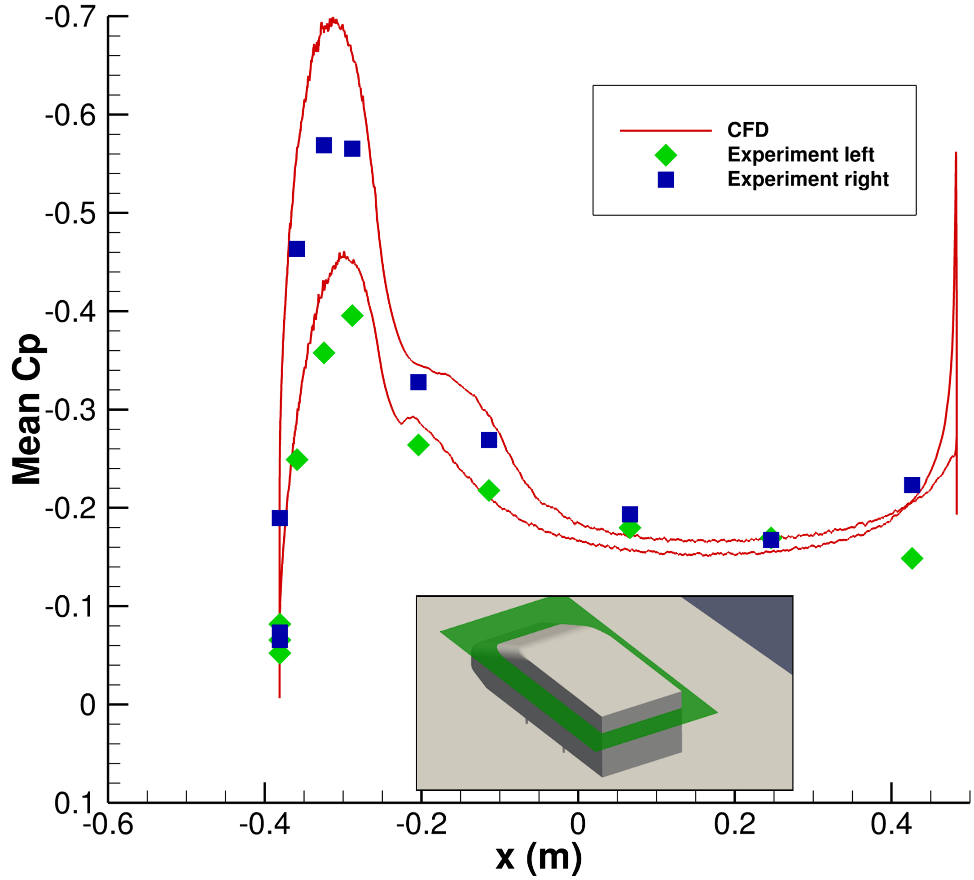

Fig. 6 Comparison of pressure coefficient at $z = 0.2595\,\mathrm{m}$ for the Windsor body.

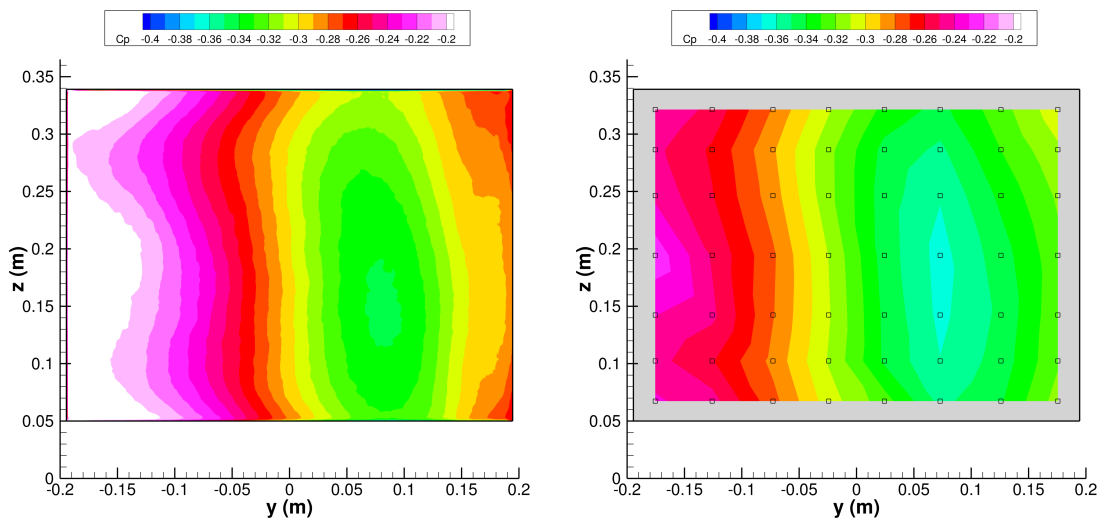

Fig. 7 Left: time-averaged pressure coefficient at the base of the Windsor body. Right: comparison of time-averaged pressure coefficient at the base of the Windsor body.

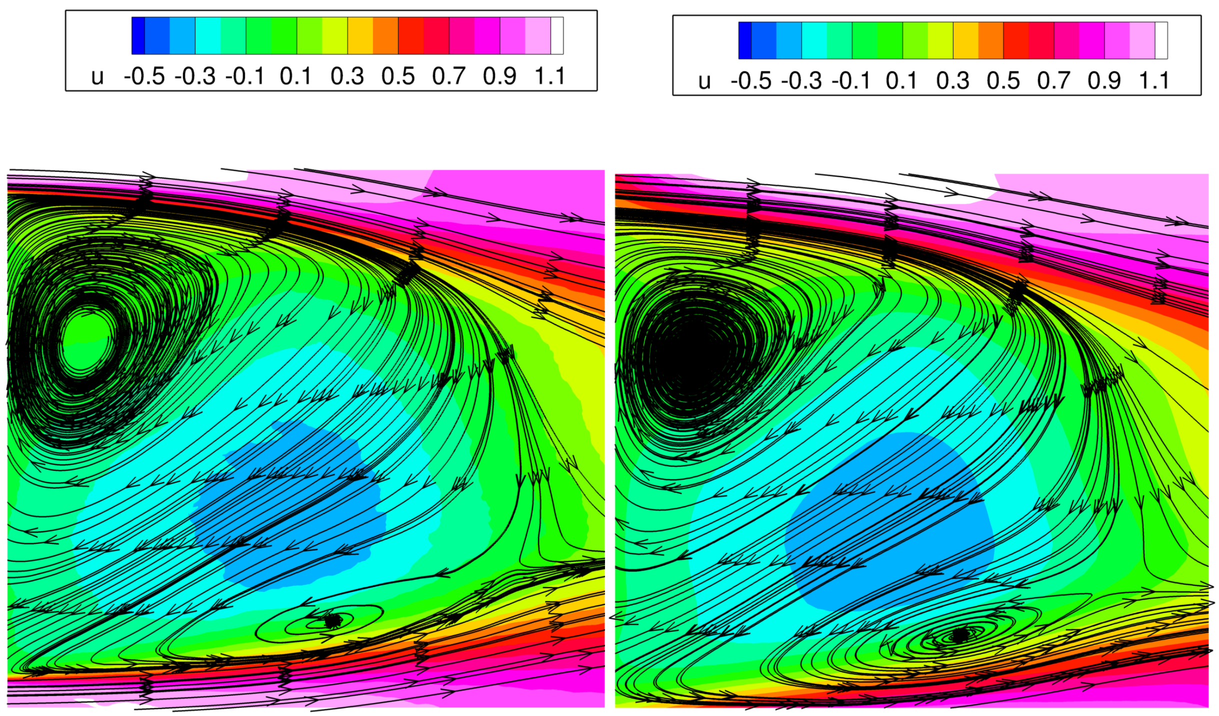

Fig. 8 Comparison of mean velocity streamlines colored by normalized streamwise velocity at $z = 0.195$ m for the Windsor body. CFD results are shown on the left and the experiment data is plotted on the right.

.

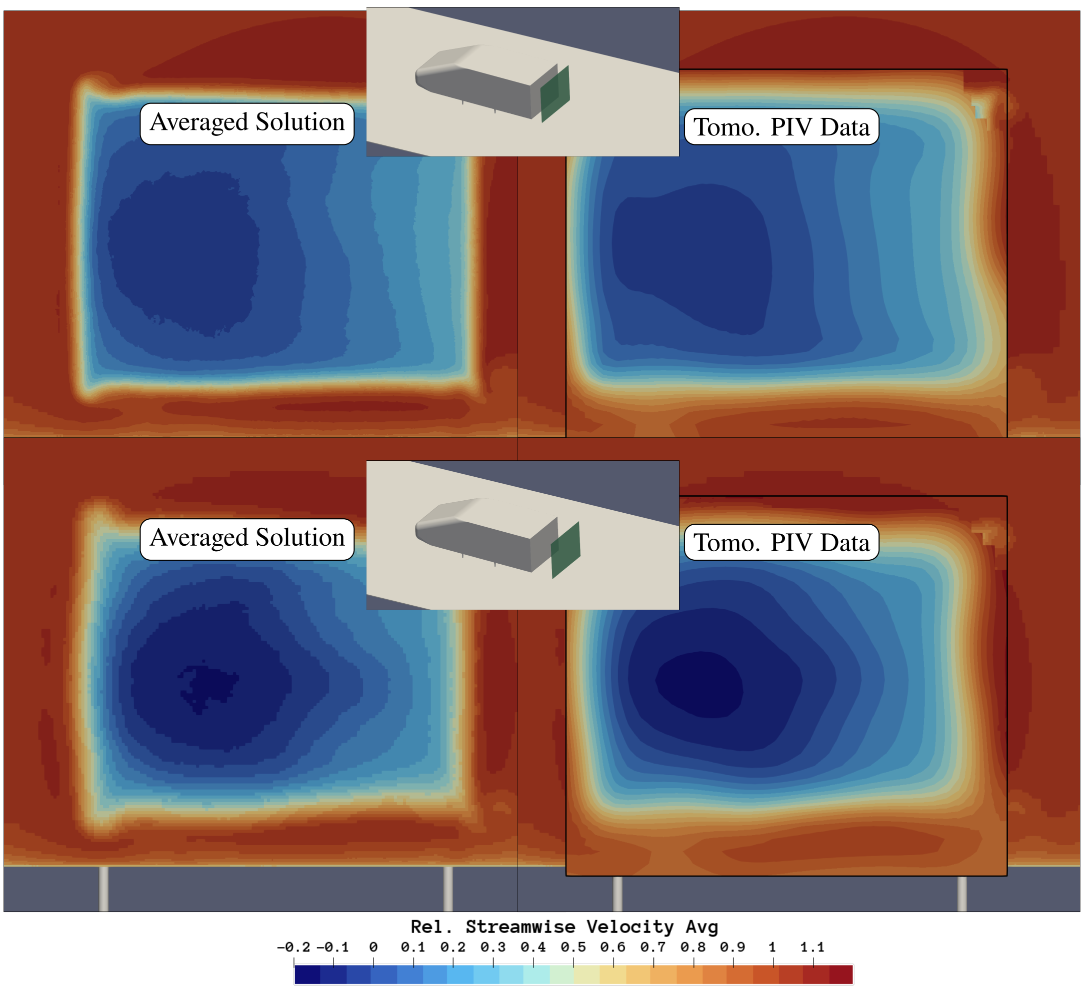

Fig. 9 Time-averaged streamwise velocity at $x = 0.578$ m **(top) and** $x = 0.670\,48$ m **(bottom).**

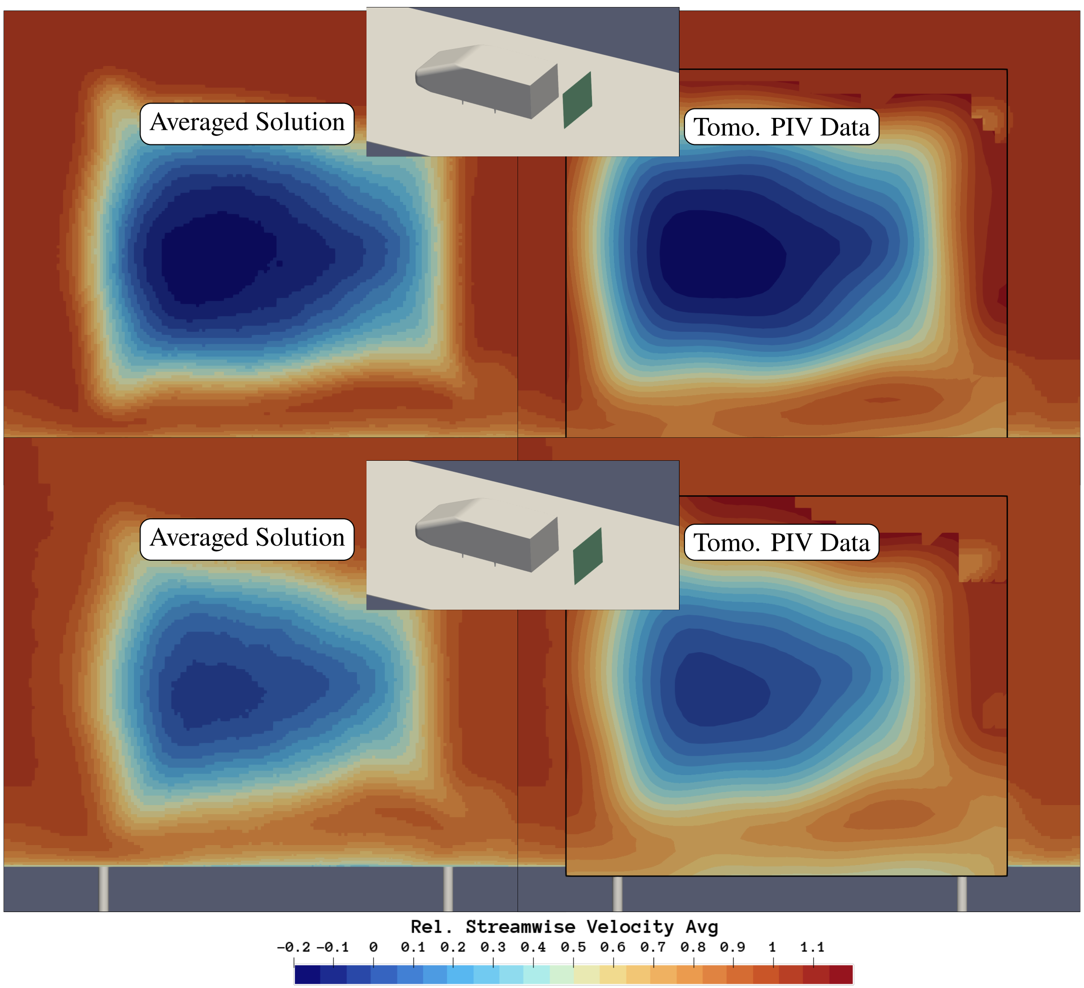

Fig. 10 Time-averaged streamwise velocity at $x = 0.774\,52$ m **(top) and** $x = 0.867$ m **(bottom).**

B. Case 2a and 2b: DrivAer

The DrivAer model [9, 10] has become a standard benchmark for automotive aerodynamics due its frequent testing and consistent results in different wind tunnels. It supports multiple configurations but for AutoCFD 3 and 4, the configuration considered is the DrivAer Notchback with closed cooling [11]. This case is a large step in complexity from the Windsor body with most features of modern passenger cars being present. Test results and a thorough description of the case and data can be found in [11]. The flow conditions are provided in the AutoCFD4 Case 2 problem description[§]. Table 2 summarizes the given conditions and some derived quantities.

Table 2 Freestream and derived conditions from the Case 2 problem description.

Density $[kg/m^3]$	Vel. mag. [m/sec]	Temp. [K]	Length (car) [m]	Reynolds number [-]	Mach number [-]	CTU [sec]
1.204	38.8889	293.23	4.6128	11.9×10^6	0.11	0.12

Figure 11 shows the computational domain and the boundary conditions. The inflow is set using total pressure and temperature conditions based on the Mach number in Table 2. A static pressure is prescribed at the outflow boundary which is slightly adjusted (approximately 30 Pa) from the standard atmospheric condition to achieve the experimental freestream velocity. The floor is modeled with an upstream inviscid portion. The purpose of this is to reflect the suction and tangential blowing that was used in the experiment by not allowing an upstream boundary layer to develop in the simulations. This portion transitions suddenly to a no-slip floor since the experiment was conducted without a road belt system meaning the floor was stationary.

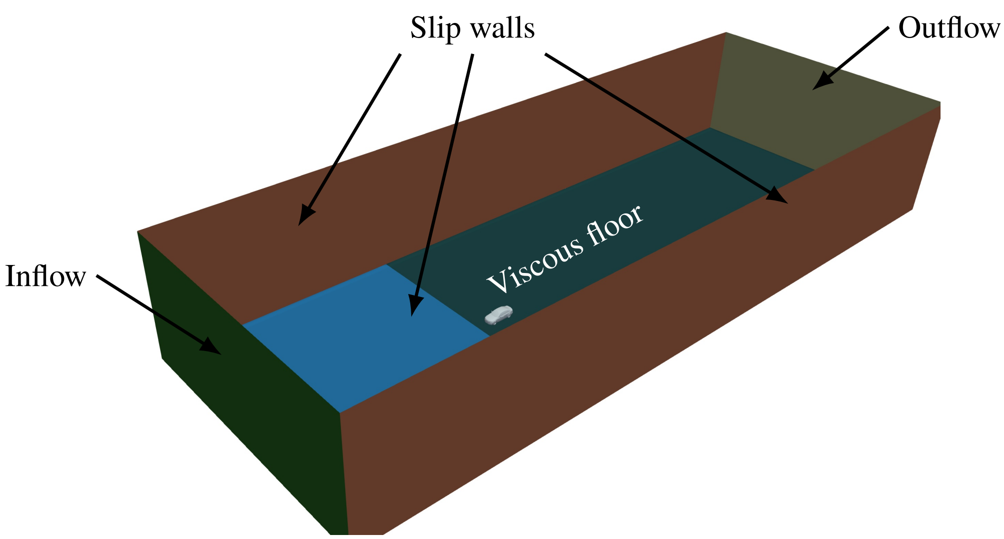

Fig. 11 Overview of the domain defined by the AutoCFD problem description.

A graphical overview of the mesh is shown in Figure 12. A global view is given with some representative slices colored by their grid spacing. The darkest red color indicates the minimum grid spacing with each subsequent neighboring level being a factor of two coarser. There are targeted surface refinement regions near the nose and front wheels with additional volume refinement behind the car to resolve the recirculation. The minimum grid spacing $\Delta x_{\min}$ and the grid level topology are sufficient to define the total grid structure so the phrase 1 mm grid[¶] should be understood to mean a mesh with 1 mm as the finest grid level and with the topology depicted in Figure 12. A matrix of runs were conducted considering variations for the subgrid scale model and the minimum grid spacing. Vreman and dynamic Smagorinsky (DSM) subgrid scale models are tested for a 2 mm and 1 mm grid considering Case 2a and Case 2b for a total of eight simulations. A coarse mesh for Case 2a is constructed and run to generate an initial condition for all other

§ `autocfd.org`

¶ The word mesh or grid is used interchangeably.

Table 3 Computational cost for the DrivAer meshes used in this section. All simulations were run using a single Amazon EC2 g5.48xlarge node (containing 8× NVIDIA A10g GPUs)

Min. grid spacing [mm]	No. of compute cells [M]	Wall time / CTU [min]
2	375	69
1	535	192

simulations. For each simulation, the coarse solution is interpolated onto the mesh and time stepping proceeds for five CTU before sampling begins to time average quantities. Table 3 provides some details about the size of the meshes the time to run the cases (based on the 2a variant with Vreman model, differences are negligible).

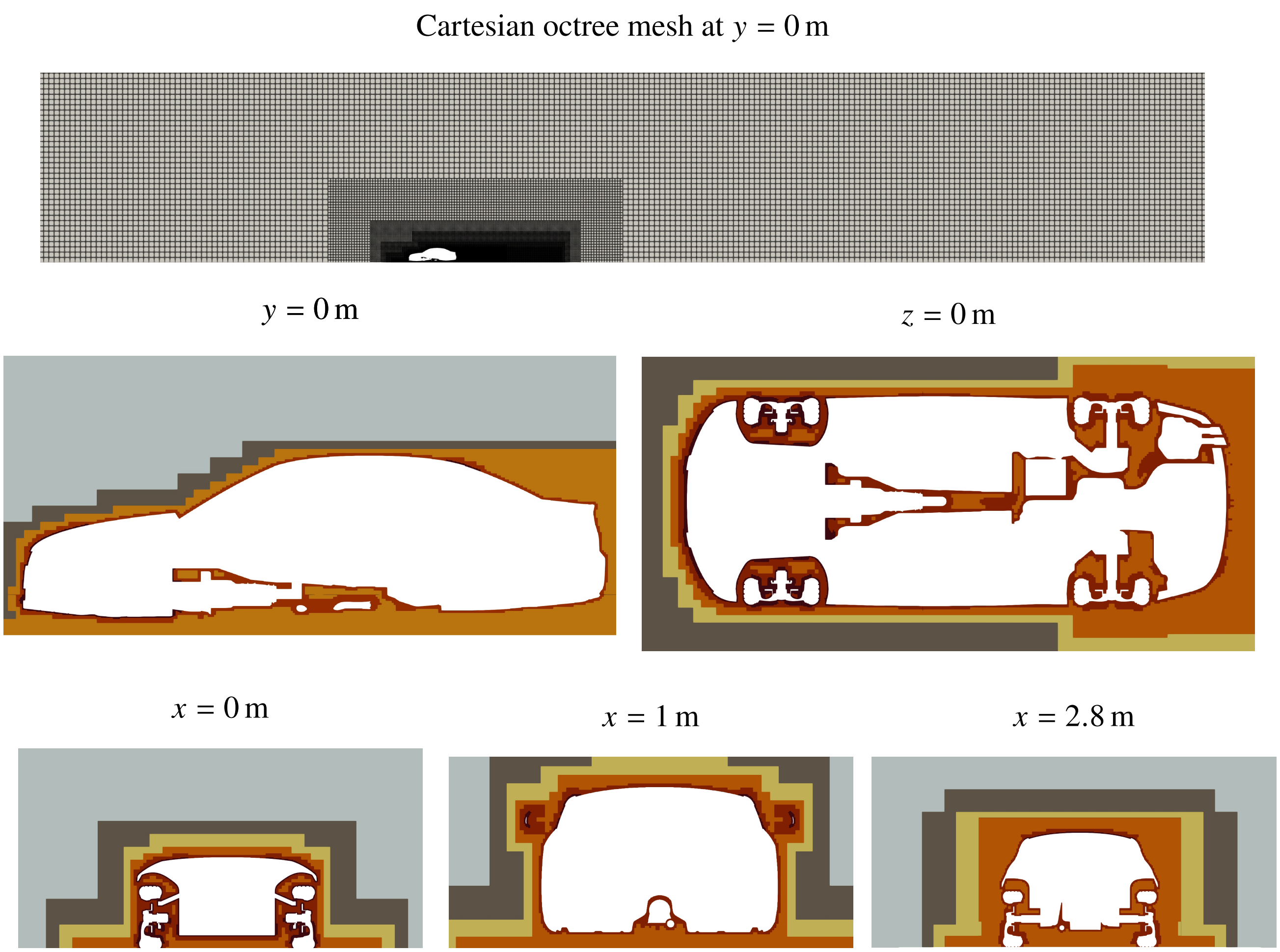

Fig. 12 Top: A global view of the $y = 0$ plane showing the octree mesh. Middle and Bottom: Coordinate slices at different representative locations to show the grid refinement topology. The darkest red near the nose, front wheels, and rear windshield represent the finest grid spacing.

1. Case 2a

Figure 13 shows the location of a subset of the pressure taps used in the experiment as well the measurement stations for a subset of the velocity profiles used to make comparisons in this section. In Figure 14 we compare both subgrid

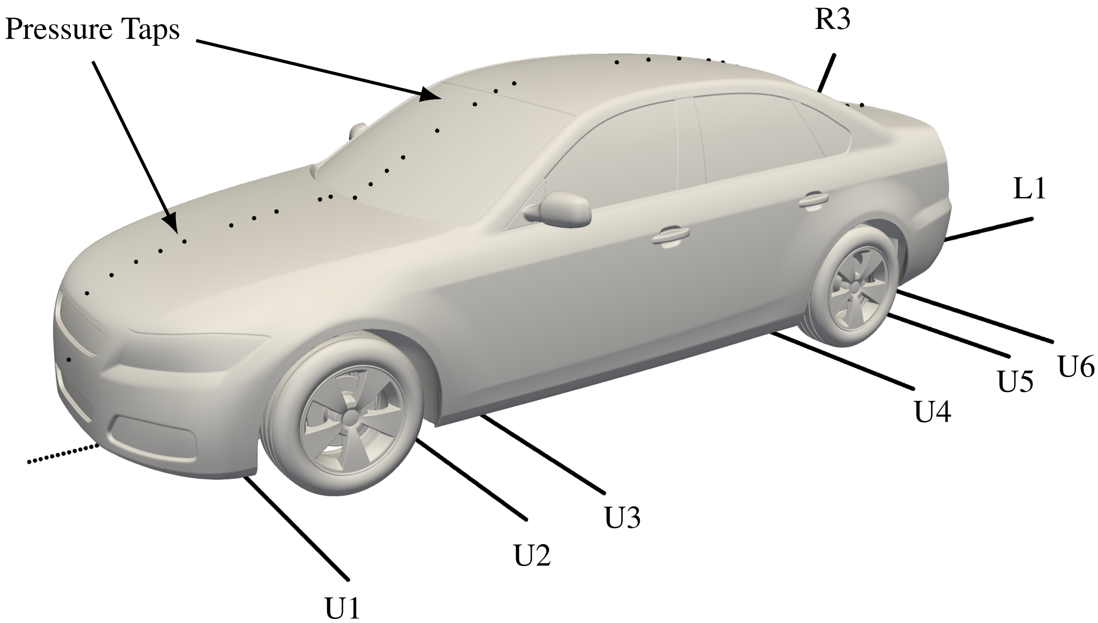

Fig. 13 Diagram of the locations for the pressure sensors on the upper body centerline and the velocity stations. The black dots on the car indicate where experimental pressure data is measured for comparisons shown in Figures 14, 16,and 16. The black lines indicate the stations used for velocity profile comparisons in Figure 17.

scale models using the 1 mm grid by plotting average C_p on the upper body centerline. The solutions agree nearly everywhere except near $x \approx 3.3$ m at the base of the rear windshield. The simulation using the Vreman model shows a larger overprediction "bump" in C_p compared to the DSM results. An overprediction in C_p at this location is consistent with other DrivAer simulations and the improvement here is significant. Based on this, DSM is considered the preferred subgrid scale model and details of the Vreman model simulations are omitted except for the velocity profiles in Figure 17 where the Vreman model results are included specifically to compare profiles at the location of the C_p difference (R3 in Figure 13). Figure 15 shows a comparison of drag history for the 2 mm and 1 mm Case 2a simulations using DSM. The finer resolution 1 mm grid shows a reduced drag which is in the direction of the experimental value of $C_{d,\mathrm{exp}} = 0.255$ but overpredicted. However, an overprediction of drag is consistent with many DrivAer simulations from the prior AutoCFD2 and AutoCFD3 workshops [‖]. For these same two simulations, Figure 16 shows average C_p on the upper and lower centerlines of the geometry. There is no clear difference on the upper portion of the car but, underneath the car, which has significantly more complex geometric features, there is an obvious improvement from the finer mesh resolution. These trends are encouraging however, notably missing is a third finer mesh to determine how near the 1 mm solution is to a "grid converged" solution which is planned as near-future work. Lastly, before moving on to compare the 2a and 2b variants, Figure 17 shows an array of line plots comparing the 2 mm mesh using DSM and the 1 mm mesh using both Vreman and DSM. Focusing on the L1 station, the main difference is the wake region with the 1 mm DSM solution showing less fall-off compared to the 2 mm DSM. There are almost no differences between the 1 mm Vreman and DSM results besides R3, as mentioned previously. There is no velocity data available at R3 but the C_p improvement at this location suggests that the DSM is more accurate. U1 is mostly steady, being upstream of the car, and does not show any difference between the approaches. The remaining profiles (U2-U6) are less well predicted than L1, however these profiles are also the most unsteady and show significant spread among previous workshop submissions. Regardless, some previous AutoCFD submissions have managed to achieve agreement at these stations and improving the results here offers some remaining work.

[‖] https://autocfdv3.s3.eu-west-1.amazonaws.com/presentations/Th1105_AutoCFD3_Case2_Results_220421_PUBLISHED.pdf

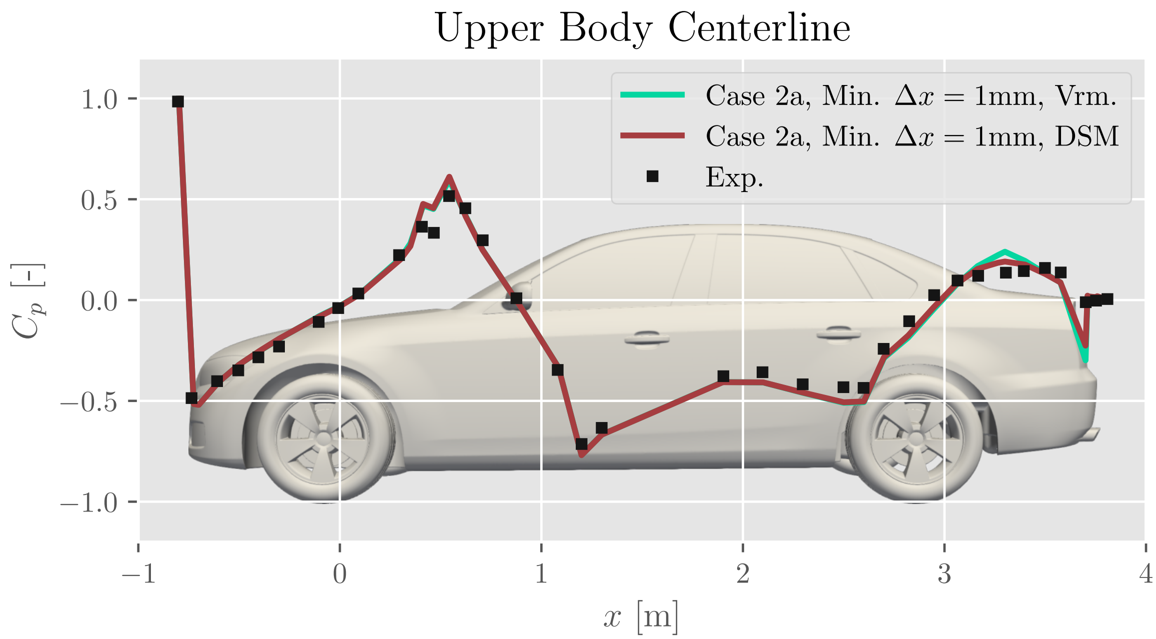

Fig. 14 Line plot of C_p along the upper body probes comparing subgrid scale models for the 1 mm grid. The only location with a noticeable difference at the base of the rear windshield where DSM matches the experiment more closely.

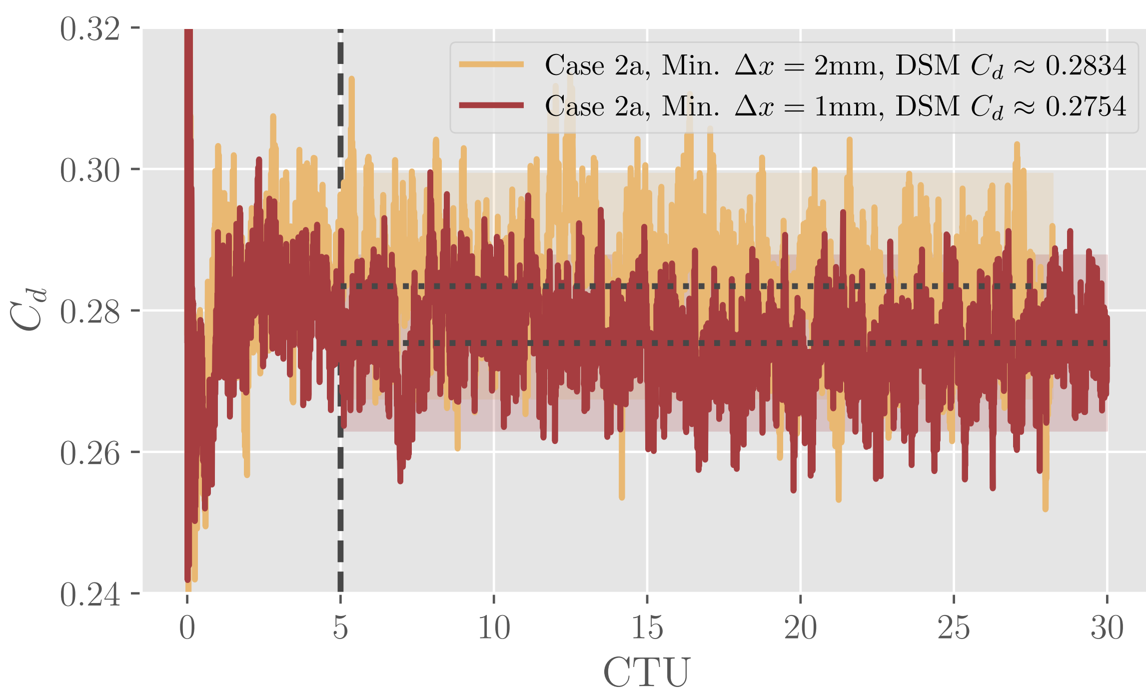

Fig. 15 Drag history for 2 mm and 1 mm grids using the dynamic Smagorinsky model (DSM). The vertical dashed line indicates the start of time averaging. The horizontal dashed lines show the computed mean.

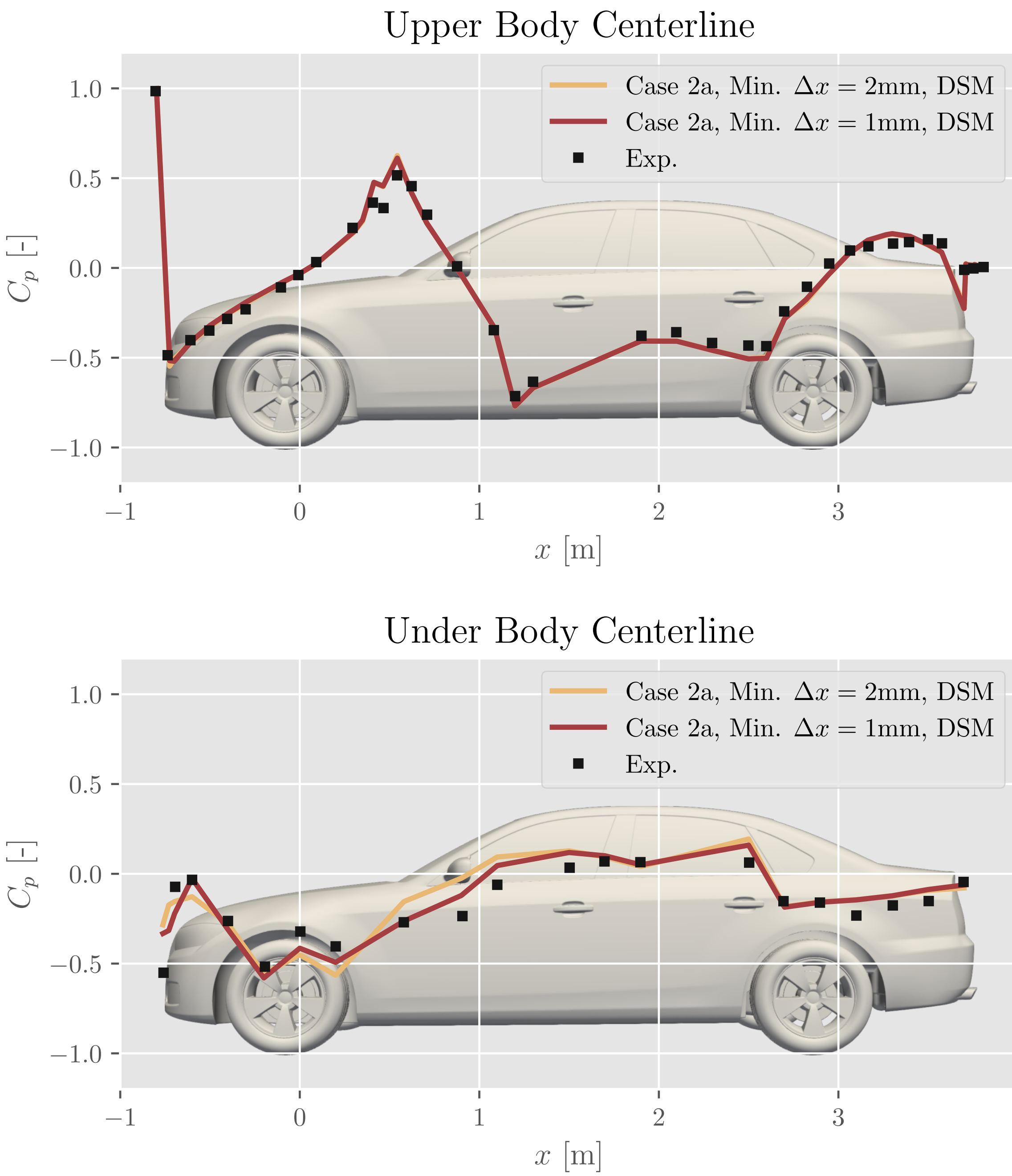

Fig. 16 Upper and lower body C_p plots for 2 mm and 1 mm meshes. On top of the car, there is no meaningful difference but the underbody probes show improved accuracy near the front of the car where there is targeted surface refinement.

2. Case 2b and Comparisons

As previously mentioned, the purpose of the Case 2 variants is to predict aerodynamic differences due to design changes. To better appreciate the influence of the front wheel deflector (FWD), Figure 18 shows the front body and wheel colored by time averaged C_p. Here the reduction in drag due to the FWD is seen as a largely reduced C_p on the front wheels which are a significant contributor of drag. Table 4 summarizes the average drag coefficient for all simulations considered in this section. The columns and rows specify the choice of subgrid scale model and mesh

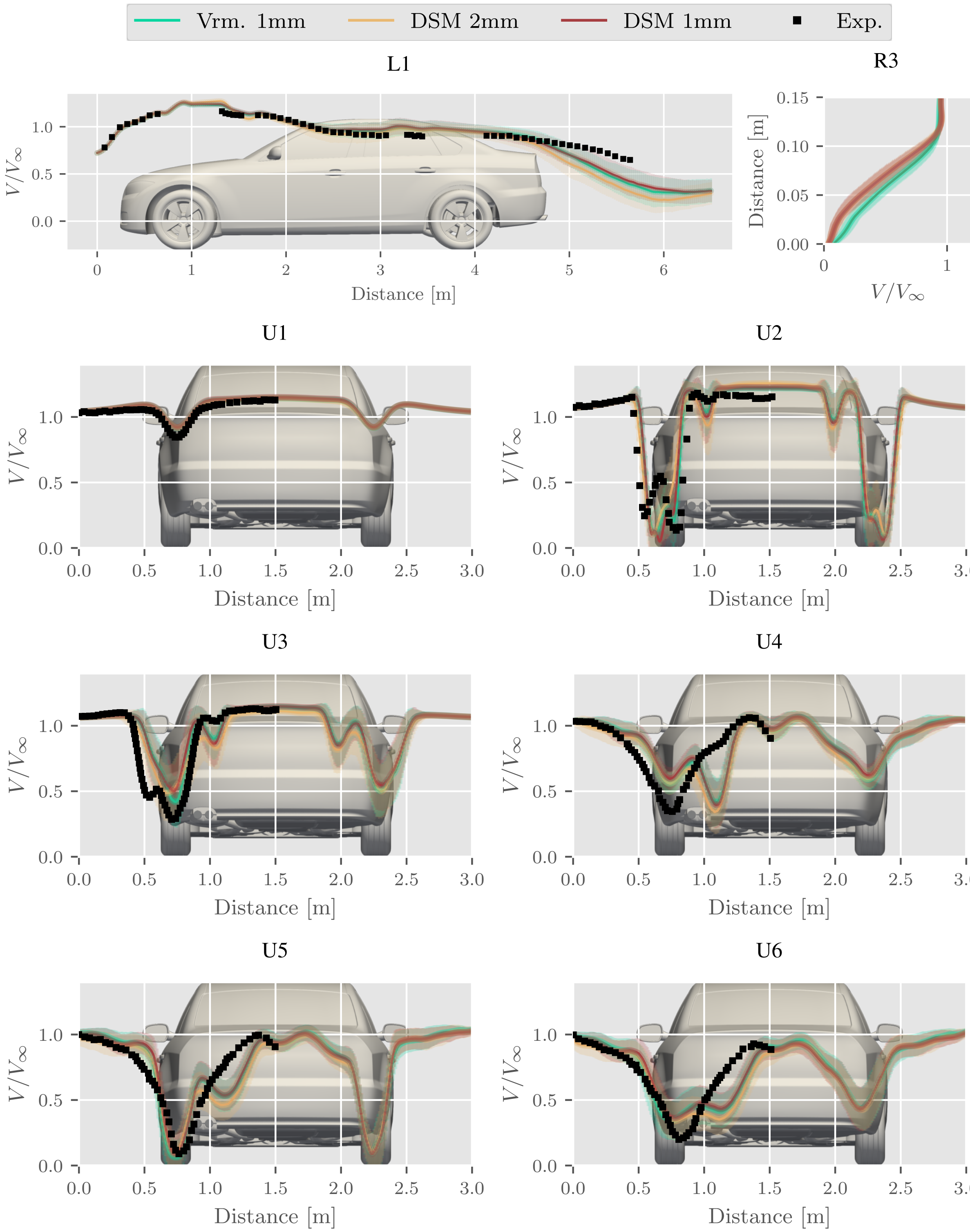

Fig. 17 Velocity profiles comparing 2 mm and 1 mm meshes for DSM and the 1 mm mesh for the Vreman model. Vreman is included to emphasize the difference in velocity at R3 which is reflected in C_p. For DSM simulations, there is an improvement to the velocity drop-off in L1 with mesh refinement. Other profiles are arguably better with refinement or largely the same for both grids.

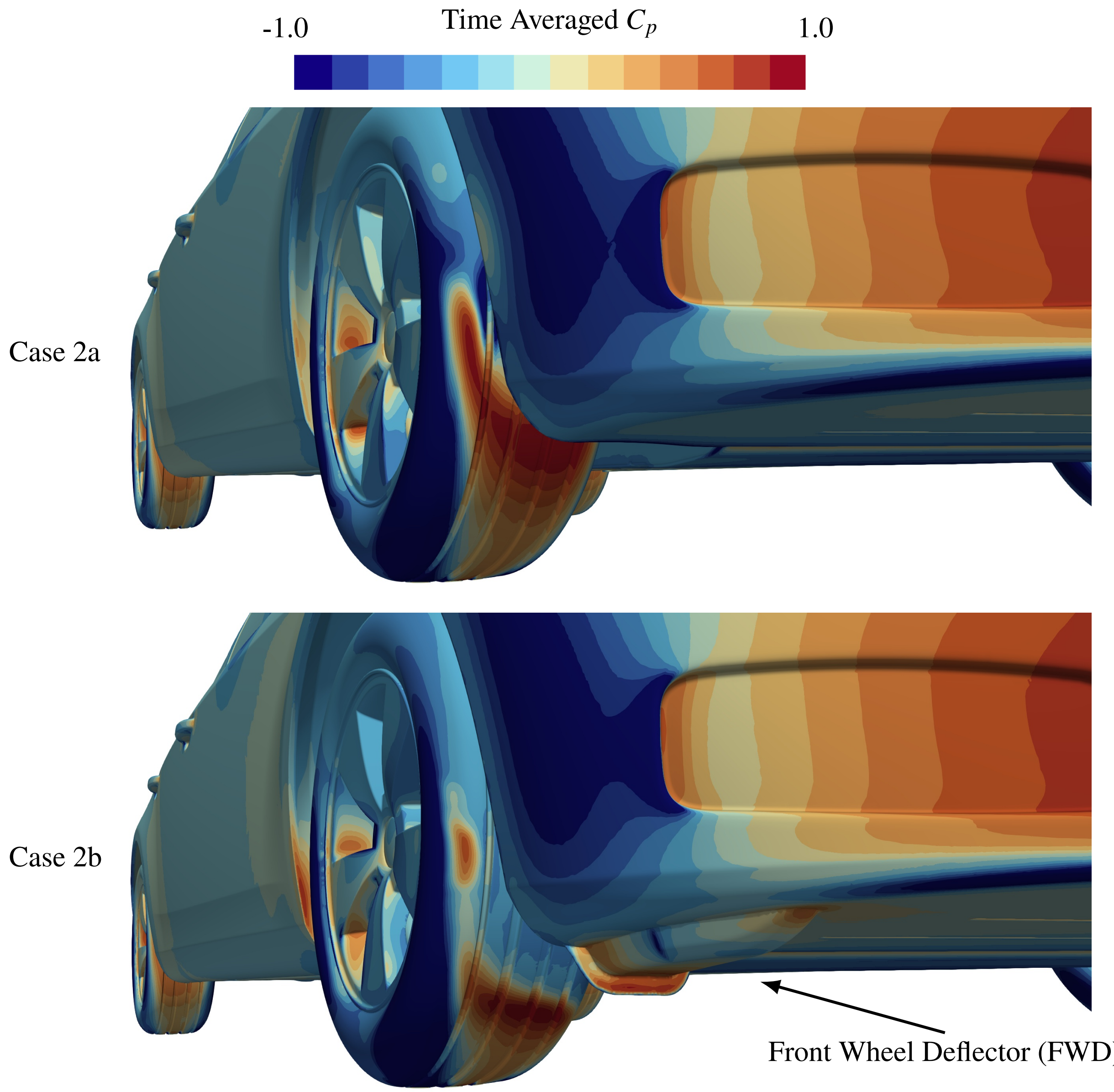

Fig. 18 Case 2a and 2b variants colored by time averaged C_p showing the reduced C_p on the wheel.

Table 4 Drag coefficient for all eight simulations.

$\Delta x_{\min}$	C_d (2a)		C_d (2b)		ΔC_d	
	Vreman	DSM	Vreman	DSM	Vreman	DSM
2 mm	0.2812	0.2834	0.2736	0.2740	0.0076	0.0094
1 mm	0.2765	0.2754	0.2650	0.2647	0.0115	0.0107

spacing which are grouped by the geometry variant. The drag coefficient shows practically no sensitivity to the subgrid scale model which is consistent with the previous observations where only a highly localized difference was observed in C_p. The last column indicates the ΔC_d where by comparing the rows it is seen that the 1 mm grid ΔC_d is quite close the

the measured value of $\Delta C_{d,\mathrm{exp}} \approx 0.0126$. Figure 19 shows two line plots of drag history for the 2 mm (top) and 1 mm (bottom) grids. The legend indicates the C_d value for each simulation and the ΔC_d values are shown to the right of the plots. Again, it remains as future work to pursue another level of mesh refinement to see that this favorable trend persists for smaller grid spacings.

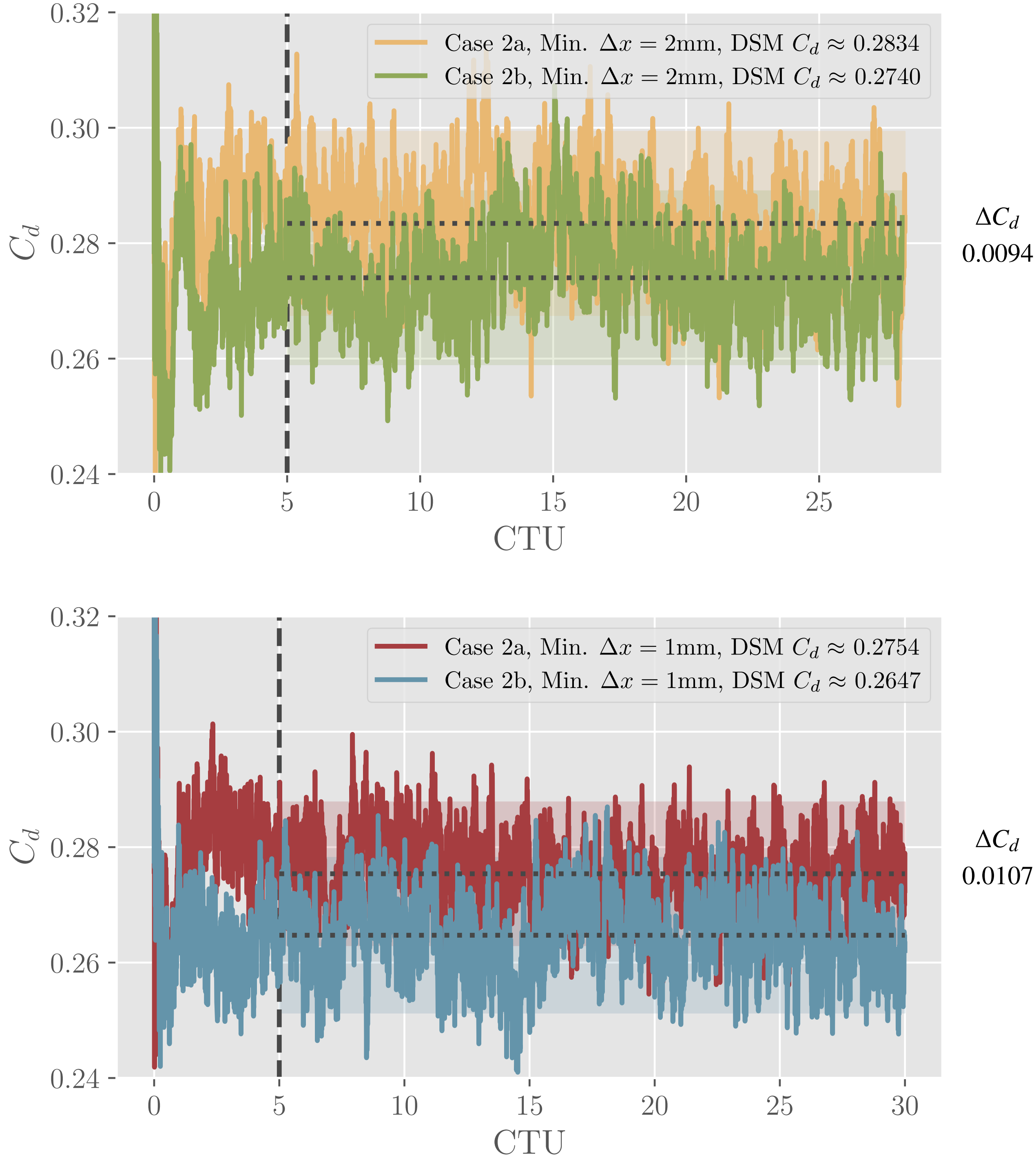

Fig. 19 Drag history and ΔC_d of Cases 2a and 2b for the 2 mm and 1 mm grids. Grid refinement increases ΔC_d to better agree with the experimental value 0.012.

IV. Summary

Preliminary results for two AutoCFD4 cases are presented using a new Cartesian immersed boundary Wall-Modelled Large Eddy Simulation (WMLES) approach. The aim of this work is to provide one perspective on the current practical feasibility for applying Cartesian octree-based WMLES to industrial automotive design problems. The favorable comparisons for Windsor body and DrivAer Notchback body were achieved using a single Amazon EC2 g5.48xlarge node, containing just 8× Nvidia A10g GPUs. Because of the low memory requirement of the Cartesian octree approach, simulations of several hundred million grid cells fit easily on relatively inexpensive and readily available hardware. The affordability makes it feasible to run these simulations routinely on a conventional workstation or many in parallel on a cloud service or an on-premises cluster. Future work will be to continue the mesh refinement study for the DrivAer model to establish a clear set of best practices for the automotive community.

Acknowledgments

The authors would like to thank the organizers of the 4th Automotive CFD Prediction Workshop (AutoCFD 4) for providing all necessary data to perform the simulations and their work to create and maintain the community effort. We would also like to thank Dr. Burkhard Hupertz, Dr. Gary Page, and Dr. Charles Mockett of the organizing committee for their insightful suggestions as well as Vangelis Skaperdas for creating the surface triangulations that were used in all of the simulations in this paper. Additionally, we thank Dr. Gary Page for generating several of the figures for the Windsor body simulations.

References

[1] Hucho, W. H., and Sovran, G., "Aerodynamics of road vehicles," 1993, pp. 485–537.

[2] Spalart, P. R., Deck, S., Shur, M. L., Squires, K. D., Strelets, M. K., and Travin, A., "A New Version of Detached-eddy Simulation, Resistant to Ambiguous Grid Densities," *Theor. Comput. Fluid Dynam.*, Vol. 20, No. 3, 2006, pp. 181–195. https://doi.org/10.1007/s00162-006-0015-0.

[3] Ashton, N., Unterlechner, P., and Blacha, T., "Assessing the Sensitivity of Hybrid RANS-LES Simulations to Mesh Resolution, Numerical Schemes and Turbulence Modelling within an Industrial CFD Process," *SAE Technical Papers*, Vol. 2018-April, 2018. https://doi.org/10.4271/2018-01-0709.

[4] Ashton, N., West, A., Lardeau, S., and Revell, A., "Assessment of RANS and DES methods for realistic automotive models," *Computers & Fluids*, Vol. 128, 2016, pp. 1–15. https://doi.org/10.1016/j.compfluid.2016.01.008, URL http://linkinghub.elsevier.com/retrieve/pii/S0045793016000190.

[5] Ashton, N., and Van Noordt, W., "Overview and Summary of the First Automotive CFD Prediction Workshop: DrivAer Model," *SAE International Journal of Commercial Vehicles*, Vol. 16, No. 1, 2022. https://doi.org/10.4271/02-16-01-0005.

[6] Hupertz, B., Lewington, N., Mockett, C., Ashton, N., and Duan, L., "Towards a Standardized Assessment of Automotive Aerodynamic CFD Prediction Capability - AutoCFD 2: Ford DrivAer Test Case Summary," *SAE Technical Papers*, SAE International, 2022. https://doi.org/10.4271/2022-01-0886.

[7] Page, G. J., and Walle, A., "Towards a Standardized Assessment of Automotive Aerodynamic CFD Prediction Capability - AutoCFD 2: Windsor Body Test Case Summary," *SAE Technical Papers*, SAE International, 2022. https://doi.org/10.4271/2022-01-0898.

[8] Varney, M., "Base drag reduction for squareback road vehicles," Ph.D. thesis, 2020. https://doi.org/https://doi.org/10.26174/thesis.lboro.11823759.v1.

[9] Heft, A. I., Indinger, T., and Adams, N. A., "Introduction of a New Realistic Generic Car Model for Aerodynamic Investigations," *SAE*, 2012. https://doi.org/10.4271/2012-01-0168.

[10] Heft, A. I., and Adams, N. A., "Experimental and numerical investigation of the drivaer model," *Proceedings of the ASME 2012 Fluids Engineering Summer meeting*, 2012, pp. 1–11.

[11] Hupertz, B., Chalupa, K., Krueger, L., Howard, K., Glueck, H.-d., Company, F. M., Chang, J.-h., Hyundai, Y.-s. S., and Company, M., "On the Aerodynamics of the Notchback Open Cooling DrivAer: A Detailed Investigation of Wind Tunnel Data for Improved Correlation and Reference," *SAE Technical Papers*, , No. 2021-01-0958, 2021, pp. 1–22. https://doi.org/10.4271/2021-01-0958.

[12] Ahmed, S. A., and Giddens, D. P., "Pulsatile poststenotic flow studies with laser Doppler anemometry," *Journal of Biomechanics*, Vol. 17, No. 9, 1984, pp. 695–705.

[13] Gottlieb, S., and Shu, C.-W., "Total variation diminishing Runge-Kutta schemes," *Mathematics of computation*, Vol. 67, No. 221, 1998, pp. 73–85.

[14] Vreman, A., "An eddy-viscosity subgrid-scale model for turbulent shear flow: Algebraic theory and applications," *Physics of fluids*, Vol. 16, No. 10, 2004, pp. 3670–3681.

[15] Moin, P., Squires, K., Cabot, W., and Lee, S., "A dynamic subgrid-scale model for compressible turbulence and scalar transport," *Physics of Fluids A: Fluid Dynamics*, Vol. 3, No. 11, 1991, pp. 2746–2757.

[16] Lilly, D., "A proposed modification of the germano sugrid-scale closure method," *Phys Fluids A*, Vol. 4, 1992, pp. 633–635.

[17] Wong, M. L., Ghate, A. S., Kenway, G. K. W., Angel, J. B., and Kiris, C. C., "Immersed Boundary Wall-Modelled Large Eddy Simulations of Straight Wings with Three-Dimensional Ice Accretion," *AIAA Aviation 2024 Forum*, 2024.

[18] Angel, J. B., Ghate, A. S., Kenway, G. K. W., Wong, M. L., Browne, O. M. F., and Kiris, C. C., "Validation of Immersed Boundary Wall-Modelled Large Eddy Simulations with F-16XL Flight Data," *AIAA Aviation 2024 Forum*, 2024.

[19] Wong, M. L., Ghate, A. S., Kenway, G. K. W., Angel, J. B., and Kiris, C. C., "Immersed Boundary Wall-Modelled Large Eddy Simulations of Subsonic Jet Flows and Acoustics," *AIAA Aviation 2024 Forum*, 2024.

[20] Wong, M. L., Ghate, A. S., Kenway, G. K. W., Angel, J. B., and Kiris, C. C., "Immersed Boundary Wall-Modelled Large Eddy Simulations of a Nose Landing Gear for Aeroacoustics," *AIAA Aviation 2024 Forum*, 2024.

[21] Kenway, G. K. W., Ghate, A. S., Browne, O. M. F., Wong, M. L., Angel, J. B., and Kiris, C. C., "Immersed Boundary Wall-Modelled Large Eddy Simulations of a Generic Hammerhead Payload Fairing," *AIAA Aviation 2024 Forum*, 2024.

[22] Ashton, N., Angel, J., Ghate, A., Kenway, G., Long Wong, M., Kiris, C., Walle, A., Maddix, D., and Page, G., "WindsorML - High-Fidelity Computational Fluid Dynamics Dataset for Automotive Aerodynamics," *In Review*, 2024.

[23] Varney, M., Passmore, M., Wittmeier, F., and Kuthada, T., "Experimental Data for the Validation of Numerical Methods: DrivAer Model," *Fluids*, Vol. 5, No. 4, 2020, p. 236. https://doi.org/10.3390/fluids5040236.